LAWRENCE
LIVERMORE
NATIONAL
LABORATORY

LLNL-JRNL-790302

Equation of state for a chemically dissociative, polyatomic system: carbon dioxide

C. J. Wu, D. Y. Young, P. A. Sterne, P. C. Myint

September 18, 2019

Journal of Chemical Physics

Disclaimer

The Journal of Chemical Physics

Equation of state for a chemically dissociative, polyatomic system: Carbon dioxide

Cite as: J. Chem. Phys. **151**, 224505 (2019); https://doi.org/10.1063/1.5128127
Submitted: 16 September 2019 . Accepted: 20 November 2019 . Published Online: 11 December 2019

Christine J. Wu, David A. Young, Philip A. Sterne, and Philip C. Myint

The Journal of Chemical Physics ARTICLE scitation.org/journal/jcp

Equation of state for a chemically dissociative, polyatomic system: Carbon dioxide

Cite as: J. Chem. Phys. 151, 224505 (2019); doi: 10.1063/1.5128127
Submitted: 16 September 2019 • Accepted: 20 November 2019 •
Published Online: 11 December 2019

Christine J. Wu,[a] David A. Young, Philip A. Sterne, and Philip C. Myint

AFFILIATIONS

Physics Division, Lawrence Livermore National Laboratory, Livermore, California 94550, USA

[a]Electronic mail: wu5@llnl.gov

ABSTRACT

A notorious challenge in high-pressure science is to develop an equation of state (EOS) that explicitly treats chemical reactions. For instance, many materials tend to dissociate at high pressures and temperatures where the chemical bonds that hold them together break down. We present an EOS for carbon dioxide (CO_2) that allows for dissociation and captures the key material behavior in a wide range of pressure–temperature conditions. Carbon dioxide is an ideal prototype for the development of a wide-ranging EOS that allows for chemical-dissociation equilibria since it is one of the simplest polyatomic systems and because it is of great interest in planetary science and in the study of detonations. Here, we show that taking dissociation into account significantly improves the accuracy of the resulting EOS compared to other EOSs that either neglect chemistry completely or treat CO_2 dissociation in a more rudimentary way.

I. INTRODUCTION

A well-known challenge in building an equation of state (EOS) is the inclusion of chemical dissociation, yet this is essential for modeling many materials in which the dissociation reactions constitute a sizable contribution to changes in the total free energy. Dissociation is especially important in polyatomic systems such as polymers, foams, and various types of molecular compounds.[1–4] Both high temperatures and pressures can induce chemical transformations. Ignoring the chemistry (i.e., bond breakage and evolution of species) may result in significant errors in describing the compression behavior as well as thermal response of these materials, as we will demonstrate throughout this study.

The main objective of this paper is to develop a dissociation-aware EOS for carbon dioxide (CO_2) that covers a global range, i.e., densities and temperatures spanning from 10^{-7} to 10^{3} g/cc and 1 to 10^{9} K, respectively. To achieve this, we have generalized the previously proposed dissociation methodology for diatomic species[5] to polyatomic systems. We aim to cover multiple domains appropriate for a variety of applications with our CO_2 EOS. For example, at lower pressures and temperatures (in the context of the gaseous and liquid conditions depicted in Fig. 1), CO_2 plays an important role in global warming and climate change,[6–8] as well as industrial processes involving combustion, organic synthesis, and improved oil recovery.[9,10] Carbon dioxide also has numerous applications at higher pressures and temperatures, including conditions where chemical dissociation is prominent. It is a common detonation product of high explosives (e.g., TNT, RDX, and HMX).[11] Nitrogen, oxygen, and carbon—as well as perhaps CO_2—are key constituents of the interiors of Uranus and Neptune.[12] Finally, CO_2 plays an important role in Earth's geochemical carbon cycle,[13,14] including in oxidization processes of mantle materials.[15]

However, the chemical behavior exhibited by CO_2 can be complex and sometimes inconsistently reported, especially for solid phases.[12–24] Broadly speaking, one may divide the CO_2 solid phases into two categories: molecular and polymeric solids. It is meaningless to speak of individual molecules in the polymeric solids and is more appropriate to imagine them as large networks of atoms connected by covalent bonds. The most well-studied polymeric solid is CO_2-V. Classifying the structure of CO_2-V has been a topic of great controversy, with the more recent studies coming to a general consensus that it has a β-cristobalite structure.[14,18,24–33] Unfortunately, the reported compressibilities of CO_2-V are not always consistent (possibly due to incomplete transformations), making it difficult to reliably model at the present time. In contrast, the molecular solids, which include phases I–IV and VII,[34–54] are composed of distinct CO_2 molecules that are held together by relatively weak intermolecular forces, not covalent bonds; as a result, their bulk moduli may

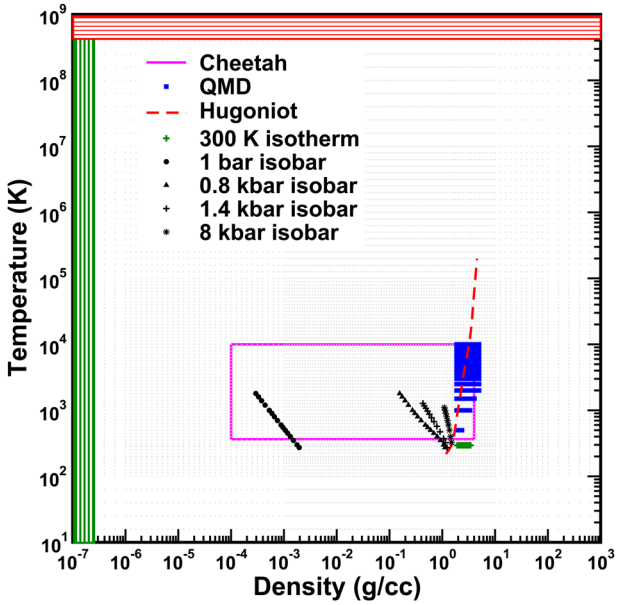

FIG. 1. Illustration of the densities and temperatures covered by our global CO_2 EOS, as well as by a representative set of experimental and theoretical constraints. The data include isobars in the fluid phases,[55] isotherms from static-compression experiments,[36] isochores from QMD simulations,[20] Hugoniot curves from QMD simulations and compression experiments,[23] and the applicable range of the Cheetah thermochemical code.[56–58] At the low densities colored in green or the high temperatures depicted in red, CO_2 behaves like an ideal gas and a fully ionized plasma, respectively.

be more than 10 times smaller than those of their polymeric counterparts. Moreover, their reported compressibilities tend to agree reasonably well, which is part of the reason why in this study we choose to focus primarily on the molecular solid phases in addition to the fluid phases.

While experimental data and atomistic simulations are invaluable toward developing an accurate EOS, they only provide information about a rather limited set of conditions, as Fig. 1 illustrates. For instance, experimental data in the form of isobars, isochores, and Hugoniot curves are short, one-dimensional segments in the much larger two-dimensional space of interest. Moreover, standard orbital-based, first-principles density functional theory (DFT) methods typically become impractical at temperatures above about 10^5 K. The thermochemical code, Cheetah,[56–58] is widely used for modeling properties under detonation conditions but only in the regimes depicted in Fig. 1, where electronic ionization is not significant. Despite these limitations, CO_2 is a relatively well-characterized system; the existing set of experiments and models, especially Cheetah, cover a significantly wider range of conditions than what we would have expected based on our previous experience with oxides and metallic compounds.

The resulting models that comprise a global EOS must provide a good representation of the available experimental and theoretical constraints, and at the same time, reproduce known physical bounds (e.g., the ideal-gas law) at the edges in Fig. 1. Here, we have attempted to develop such an EOS for CO_2 by using XEOS, which has been the workhorse EOS-generation code at Lawrence Livermore National Laboratory (LLNL) for over a decade. XEOS is built on the quotidian EOS (QEOS) methodology,[5,59,60] which describes all solid phases with a single free-energy model, and all fluid phases (liquid, vapor, and supercritical fluid) with a separate model. It makes the standard assumption that the total Helmholtz free energy can be expressed as a sum of three contributions that are referred to as the cold, ion-thermal, and electron-thermal terms. Section II describes our models for the three contributions, including an explanation of how we represent dissociation with the ion-thermal free energy. This is followed by Sec. III, which illustrates how we have constrained the model parameters with certain sets of "training data" and presents our EOS predictions for "test data" to which we have not fit the models. We conclude with a summary of this work and a proposal of how our EOS may be improved in future studies.

II. METHODOLOGY

A. Overview

In its most fundamental form, our model for the EOS is an expression of the Helmholtz energy $F(V, T)$ as a function of the temperature T and the specific volume V, which by definition is the inverse of the mass density ρ. Following the QEOS methodology,[5,59,60] $F(V, T)$ is decomposed into three free-energy contributions,

$$F(V,T) = F_{\text{cold}}(V) + F_{\text{ion}}(V,T) + F_{\text{electron}}(V,T). \tag{1}$$

This choice of decomposition is motivated by the fact that the three contributions encompass very different physics and are hence represented by markedly distinct models, as we will demonstrate below. XEOS can employ a number of models for the electron-thermal free energy, with the most common one being the Thomas–Fermi model,[59] which accounts for changes in electronic energy due to changes in density and temperature. The cold energy $F_{\text{cold}}(V)$ accounts for chemical bonding and ensures the proper cohesive energy. It represents the internal energy of the system at 0 K and thus is often called the cold curve. Finally, the ion-thermal free energy $F_{\text{ion}}(V, T)$ embodies contributions from ionic motion. It includes some combination of the translational, rotational, and vibrational modes of the ions and depends strongly on the number of species. This is also the term that explicitly accounts for chemical dissociation. Once the total free energy $F(V, T)$ is specified, all other thermodynamic properties can be determined through well-established relations, some of which are

$$S = -\left(\frac{\partial F}{\partial T}\right)_V, \tag{2}$$

$$E = F + TS = -T^2\left(\frac{\partial (F/T)}{\partial T}\right)_V, \tag{3}$$

$$P = -\left(\frac{\partial F}{\partial V}\right)_T, \tag{4}$$

where S is the entropy, E is the internal energy, and P is the pressure. In the rest of this section, we describe the functional forms we use to represent each of the three contributions. We explain how the parameters that appear in these functions may be fit to experimental data or to theoretical calculations.

B. Thomas-Fermi theory and the electron-thermal free energy

In this application of XEOS, the electron-thermal free energy is based on Thomas–Fermi (TF) theory in which a spherical volume is assumed for the atom containing Z electrons and a nucleus of charge $+Ze$. The electron cloud is modeled as a Fermi gas, and for each (V, T), the TF energy is the sum of Fermi kinetic plus electron–electron and electron–nucleus potential energies. TF theory allows one to solve for the electron density $n(r)$ as a function of the radial coordinate r subject to certain boundary conditions[59] prescribed at the radius R of the electron cloud, where R is proportional to $V^{1/3}$. This TF model permits thermodynamic functions to be scaled based on the atomic number Z and mass A. In practice, a single table for $Z = A = 1$ is stored and the scaling law is used to generate models for other elements.

Compounds are treated as mixtures of atoms for the purposes of the electron-thermal free energy. For CO_2 at pressure P and temperature T, the TF volumes of C and O atoms are found for this pressure and added to generate a total volume, $V_{\rm tot}(P, T) = V_{\rm C}(P, T) + 2V_{\rm O}(P, T)$. It is possible to do this because the TF model has no chemical bonding, and the pressure is always positive. For a given input volume $V_{\rm tot}$, this method is solved iteratively for the correct pressure. This approximation is used over the entire (V, T) range of the EOS, independently of dissociation.

TF is a highly simplified electron-thermal model with well-known weaknesses. The most noticeable deficiency is its lack of treatment for atomic shell structures. As a result, it often yields over ionization even at room temperature which leads to overestimation of heat capacity in the gas. In the shock Hugoniot, excess electron pressure leads to density maxima that are too small. In spite of its deficiencies, however, TF provides an accurate description at very high pressures and temperatures (e.g., those exceeding 10^5 K), and because of its simplicity and applicability at these extreme conditions, it has been widely used in generation of global EOSs as is the case in our study.

C. Cold energy

For this work, we have employed the published XEOS formalism[5,59] for the cold energy $F_{\rm cold}(V)$. It consists of two separate modeling regimes, one for compression ($V \le V_0$) and the other for expansion ($V > V_0$), where V_0 is the reference volume,

$$F_{\rm cold}(V) = \begin{cases} E_{\rm TF,cold}(V) + E_{\rm b}(V) + \sum_i \Delta E_i(V) + E_{\rm ref}, & V \le V_0, \\ A_{\rm c}(1/V)^{n_{\rm c}} - B_{\rm c}(1/V)^{m_{\rm c}} + E_{\rm coh} + E_{\rm b}(V) - E_{\rm b}(V \to \infty), & V > V_0. \end{cases} \tag{5}$$

For the compression regime ($V \le V_0$), as shown above, the cold curve contains multiple terms, including the repulsive TF cold energy $E_{\rm TF,cold}(V)$, an attractive bonding contribution $E_{\rm b}(V)$[59] constrained by the ambient bulk modulus, and a set of breakpoint corrections $\Delta E_i(V)$ for high pressures, the last two of which are specified as follows:

$$E_{\rm b}(V) = E_0\left(1 - \exp\left\{b\left[1 - \left(\frac{V}{V_0}\right)^{1/3}\right]\right\}\right), \tag{6}$$

$$\Delta E_i(V) = \begin{cases} A_i u_i^n/(B_i + u_i^n), & V \le V_i, \\ 0, & V > V_i, \end{cases} \tag{7}$$

where $u_i = V_i/V - 1$.

In Eq. (6), E_0 and b are positive constants that characterize the bond strength and range, respectively, which are set to yield the chosen $P = 0$ reference volume V_0 and experimental bulk modulus $B_0(V_0, T_0)$, where T_0 is the reference temperature of the solid. In Eq. (7), the parameters A_i, B_i, and n are adjustable constants that may be fit to experimental compression data. Finally, it is convenient to add a reference energy that sets the solid energy to zero at V_0 and T_0. For CO_2, the cold curve under compression is mainly constrained by the measured compressibility of the molecular solid phases for the reasons discussed in Sec. I. We set $T_0 = 196$ K and $V_0 = 1/\rho_0$, where $\rho_0 = 1.56$ g/cc, in our EOS. These conditions correspond to the molecular CO_2-I solid phase and are very close to the initial conditions in the shock-compression study by Zubarev and Telegin.[61] The pressure at T_0 and V_0 in our EOS is 1 bar.

In the expansion regime ($V > V_0$), a soft-sphere function $A_{\rm c}(1/V)^{n_{\rm c}} - B_{\rm c}(1/V)^{m_{\rm c}} + E_{\rm coh}$ is applied to ensure that $F_{\rm cold}(V \to \infty) = E_{\rm coh}$. Here, the constants $A_{\rm c}$, $B_{\rm c}$, and $m_{\rm c}$ are adjusted so that the energy, pressure, and bulk modulus are continuous at $V = V_0$. The remaining constant $n_{\rm c}$ can be adjusted to give an optimized liquid–vapor critical point. We note that Eq. (5) is used instead of more familiar analytical forms, such as the Vinet and Birch–Murnaghan equations,[62] because these analytical forms do not behave well at the extreme conditions (both at low and high densities) necessary for a global EOS.

D. Ion-thermal free energy

For a chemically dissociative system, we separate the ion-thermal free energy $F_{\rm ion}(V, T)$ into two contributions,

$$F_{\rm ion}(V, T) = F_{\rm ion,\,nd}(V, T) + F_{\rm ion,\,diss}(V, T), \tag{8}$$

in which the nondissociative term $F_{\rm ion,nd}(V, T)$ is described by separate models for the solid and fluid phases that we describe

below, and the dissociative term $F_{\text{ion,diss}}(V, T)$ is an extension of the ideal-gas dissociation model proposed by Young[5] for diatomic systems such as N_2. These two terms are coupled by the average molar mass $\tilde{M}(V, T)$, which is a function of volume and temperature because it depends on the equilibrium chemical composition of the mixture at the specified V and T. Its value ranges between the limits of 44 g/mol and 44/3 = 14.7 g/mol for the undissociated and fully dissociated cases, respectively. In other words, $\tilde{M}(V, T)$ reflects the extent of the dissociation at (V, T). Allowing $\tilde{M}$ to vary with V and T is one of the key features that distinguish dissociative systems from nondissociative ones, which have a fixed molar mass. In the rest of this section, we first present our models for the dissociative term $F_{\text{ion,diss}}(V, T)$ and follow this with a brief description of our models for the nondissociative term $F_{\text{ion,nd}}(V, T)$.

1. Dissociative term

Our phenomenological model is aimed at capturing the most important effect from dissociation, namely, the change of a material's heat capacity due to chemical reactions. Simplification is necessary given that a full description of the rather complicated dissociation behavior exhibited by CO_2 is currently out of reach. It turns out that one of the highly sensitive parameters for controlling heat capacity is the change of the average molar mass $\tilde{M}$ with V and T, which influences the system's average molar density. We have simplified the dissociation of a general polyatomic system Y into n averaged atomic species by representing this reaction with a single equation,

$$Y \rightleftharpoons nX. \tag{9}$$

In this study, Y denotes CO_2, which has a molar mass of roughly 44 g/mol, and $n = 3$ so that $X = (C + 2O)/3$ is a fictitious atomic species that has a molar mass of 44/3 = 14.7 g/mol. Following standard expressions from statistical thermodynamics,[63] we have

$$F_{\text{ion, diss}}(V, T) = -k_B T \ln Q(V, T), \tag{10}$$

where k_B is the Boltzmann constant. It is difficult to determine $Q(V, T)$ in the general case, but this problem is much more tractable if Y may be treated as though its dissociative behavior were that of an ideal gas. In this case, the partition function $Q(V, T)$ is a product of the partition functions for the individual Y and X species that obey Boltzmann statistics,

$$Q(V, T) = Q_Y(V, T) Q_X(V, T), \tag{11}$$

$$Q_Y(V, T) = \frac{q_Y(V, T)^{N_Y}}{N_Y!}, \tag{12}$$

$$Q_X(V, T) = \frac{q_X(V, T)^{N_X}}{N_X!}, \tag{13}$$

where $q_Y(V, T)$ is the single-particle partition function for Y and $N_Y = N_Y(V, T)$ is the number of Y molecules present when chemical equilibrium is established at V and T. Similar definitions apply for $q_X(V, T)$ and $N_X = N_X(V, T)$, which refer to the atomic species X.

Toward the goal of determining N_Y and N_X, we assume that our system has a total mass of 1 g at the specified V and T so that $F_{\text{ion,diss}}(V, T)$ in Eq. (10) has units of energy per gram. This means that the sum $m_Y N_Y + m_X N_X$, in which m_Y and m_X are the per-particle masses of Y and X, respectively, adds up to 1 g. In addition to this constraint on the particle numbers, we employ the following relation that is applicable to ideal gases:[63]

$$\frac{(N_X)^n}{N_Y} = \frac{(q_X)^n}{q_Y}. \tag{14}$$

Equation (14) and the constraint on the total mass $m_Y N_Y + m_X N_X$ together provide the means to compute the equilibrium composition (i.e., determine N_Y and N_X) from knowledge of the single-particle partition functions. The rest of this section on our model for $F_{\text{ion,diss}}(V, T)$ focuses on how we compute these partition functions.

Assuming that the different energy modes are independent of each other, the partition function q_Y for the molecular species Y (CO_2) may be written as a product of the partition functions for the individual modes,

$$q_Y = q_{\text{trans},Y} q_{\text{rot},Y} q_{\text{vib},Y}, \tag{15}$$

where $q_{\text{trans},Y} = q_{\text{trans},Y}(V, T)$, $q_{\text{rot},Y} = q_{\text{rot},Y}(T)$, and $q_{\text{vib},Y} = q_{\text{vib},Y}(T)$ denote the partition functions for the translational, rotational, and vibrational modes, respectively. The translational partition function is given by

$$q_{\text{trans},Y}(V, T) = \frac{V}{\Lambda_Y^3}, \tag{16}$$

in which the thermal de Broglie wavelength Λ_Y is defined as

$$\Lambda_Y = \left(\frac{h^2}{2\pi m_Y k_B T}\right)^{1/2}, \tag{17}$$

where h is Planck's constant.

In our dissociation model, we treat CO_2 as though it formed linear molecules, which is true for most of the phases, with some notable exceptions.[41,43,44,50,51,64–67] (We explain in the Conclusions how some of these exceptions may be addressed in the future by adopting a multiphase framework that allows for multiple solid phases.) The rotational partition function $q_{\text{rot},Y}$ is therefore given by

$$q_{\text{rot},Y}(T) = \sum_{j=0}^{\infty} (2j + 1) \exp\left(\frac{-j(j+1)\Theta_{\text{rot}}}{T}\right), \tag{18}$$

where $\Theta_{\text{rot}} = h^2/8\pi^2 I k_B$ is the characteristic rotational temperature and I is the moment of inertia. Since the value of Θ_{rot} is rather low for most substances (including CO_2), this expression over much of the temperature range of interest may be approximated by

$$q_{\text{rot},Y}(T) = \frac{T}{\Theta_{\text{rot}}} + \frac{1}{3} + \frac{1}{15}\frac{\Theta_{\text{rot}}}{T} + \frac{4}{315}\left(\frac{\Theta_{\text{rot}}}{T}\right)^2, \tag{19}$$

which simplifies even further to $q_{\text{rot},Y}(T) = T/\Theta_{\text{rot}}$ at sufficiently high temperatures.

For CO_2, a linear molecule, there are $3n - 5 = 4$ vibrational modes, each with a characteristic frequency ν_i. The quantum energy levels for a harmonic oscillator with frequency ν_i follow

$$\varepsilon_{ij} = \left(j + \frac{1}{2}\right) h\nu_i, \tag{20}$$

where the quantum number j ranges over 0, 1, 2, ... The vibrational partition function q_i of mode i is then

$$\begin{aligned} q_i &= \sum_{j=0}^{j_{\max}} \exp(-\varepsilon_{ij}/k_B T) \\ &= \exp(-h\nu_i/2k_B T) \sum_{j=0}^{j_{\max}} \exp(-jh\nu_i/k_B T) \\ &= \exp(-\Theta_i/2T) \sum_{j=0}^{j_{\max}} \exp(-j\Theta_i/T), \end{aligned} \tag{21}$$

where $\Theta_i = h\nu_i/k_B$ is the characteristic temperature of mode i. In summing over the vibrational states, we cut off the sum at an energy equal to the dissociation energy, corresponding to the quantum number $j_{\max}$. This prevents unrealistic high-entropy vibrational states that could stabilize CO_2 at ultrahigh temperatures. The total vibrational partition function $q_{\text{vib},Y}(T)$ is then

$$q_{\text{vib},Y}(T) = \prod_{i=1}^{4} q_i. \tag{22}$$

The atomic species X do not have any rotational or vibrational modes, but they have translational modes where the corresponding partition function $q_{\text{trans},X}(V, T)$ can again be computed from Eq. (16), with the mass m_X replacing m_Y in the thermal de Broglie wavelength. In addition, the species X are described by a dissociation term $q_{\text{diss},X} = q_{\text{diss},X}(T)$ in which

$$q_{\text{diss},X}(T) = \exp\left(-\frac{\varepsilon_{\text{diss}}}{k_B T}\right). \tag{23}$$

Because of the complex stepwise character of dissociation, we allow the dissociation energy of CO_2 to vary in order to obtain an optimal fit to EOS data. This optimal value of $\varepsilon_{\text{diss}}$ is 7.5 eV. The atomic partition function q_X may be computed from the translational and dissociation terms according to

$$q_X(V, T) = q_{\text{trans},X}(V, T) q_{\text{diss},X}(T). \tag{24}$$

2. Nondissociative term

Here, we briefly present the models used for the nondissociative term $F_{\text{ion,nd}}(V, T)$ in Eq. (8). The nondissociative and dissociative terms are coupled through the average molecular mass $\tilde{m}$, which is defined as

$$\tilde{m} = \frac{m_Y N_Y + m_X N_X}{N_Y + N_X}. \tag{25}$$

Note that $\tilde{m}$ ranges between the limits m_Y and m_X and that the average molar mass $\tilde{M}$ is related to $\tilde{m}$ and Avogadro's number N_A via $\tilde{M} = N_A \tilde{m}$. It is clear that $\tilde{m}$ and $\tilde{M}$ are functions of the equilibrium composition [specified by $N_Y = N_Y(V, T)$ and $N_X = N_X(V, T)$], which in turn depends on the extent of dissociation at V and T.

We describe $F_{\text{ion,nd}}$ of the solid phases with the well-known Debye model,[68,69] while the fluid phases are described by a model originally developed by Cowan that was later published by other authors.[59,70] The free energy of the Debye model (in terms of energy per unit mass) is

$$\begin{aligned} F_{\text{Debye}}(V, T) = &\frac{9k_B\Theta_D}{8\tilde{m}} + \frac{9k_B T}{\tilde{m}}\left(\frac{T}{\Theta_D}\right)^3 \\ &\times \int_0^{\Theta_D/T} x^2 \ln[1 - \exp(-x)]\,dx. \end{aligned} \tag{26}$$

We treat the Debye temperature $\Theta_D(V)$ as being independent of temperature so that it depends on the volume only. It is calculated by integrating the Grüneisen parameter $\Gamma(V) = -d\ln\Theta_D(V)/d\ln V$ with respect to volume V, and we represent $\Gamma(V)$ with a series of cubic splines in $\rho = 1/V$ whose coefficients are adjusted to reproduce experimental data. The solid–fluid phase boundary is given by the Lindemann criterion,[59,71] which is an empirical model which states that the transition temperature T_m for a particular volume V is

$$T_m(V) = \alpha V^{2/3} \Theta_D^2, \tag{27}$$

in which α is a material-specific constant. Let us define dimensionless variables $u = \Theta_D/T$ and $w = T_m/T$ so that Eq. (27) becomes $w/u^2 = \alpha T V^{2/3}$. The nondissociative, ion-thermal free energy of the solid phase that exists below the solid–fluid transition curve (that is, for conditions where $w > 1$) is given by the Debye model in Eq. (26). Above this curve ($w < 1$), our system will exist as a fluid. The Cowan model[59,70] that we employ to describe the nondissociative, ion-thermal free energy of this fluid phase is

$$F_{\text{Cowan}}(V, T) = \frac{k_B T}{\tilde{m}} f(u, w), \tag{28}$$

where the dimensionless function f is defined as

$$f = -\frac{11}{2} + \frac{9}{2} w^{1/3} + \frac{3}{2} \ln\left(\frac{u^2}{w}\right). \tag{29}$$

The particular QEOS variant[59] on which the XEOS code is based neglects volume changes that occur during phase transitions. This construction ensures equality of the Gibbs energy $G = F + PV$ of the solid and fluid phases along the phase boundary since their Helmholtz energies are also matched along this curve. With the neglect of volume changes, the electron-thermal contributions automatically match along the phase boundary. Furthermore, F_{Cowan} approaches the appropriate ideal-gas limit of heat capacity at high temperatures.

III. RESULTS

A. Overview

The majority of experimental data (e.g., the Hugoniot pressures) that we have used to constrain our EOS are a reflection of the total free energy of the system, which is based on the three contributions discussed in Sec. II: $F_{\text{electron}}(V, T)$, $F_{\text{cold}}(V)$, and $F_{\text{ion}}(V, T)$. Each plays a unique role in different regimes of thermodynamic phase space and subsequently contributes to the observed EOS properties in various degrees. Figure 2 displays the conditions at which each of them becomes important. As shown in Fig. 2(a), the electron-thermal term grows dramatically with temperature and dominates at high-temperature conditions due to the prominence

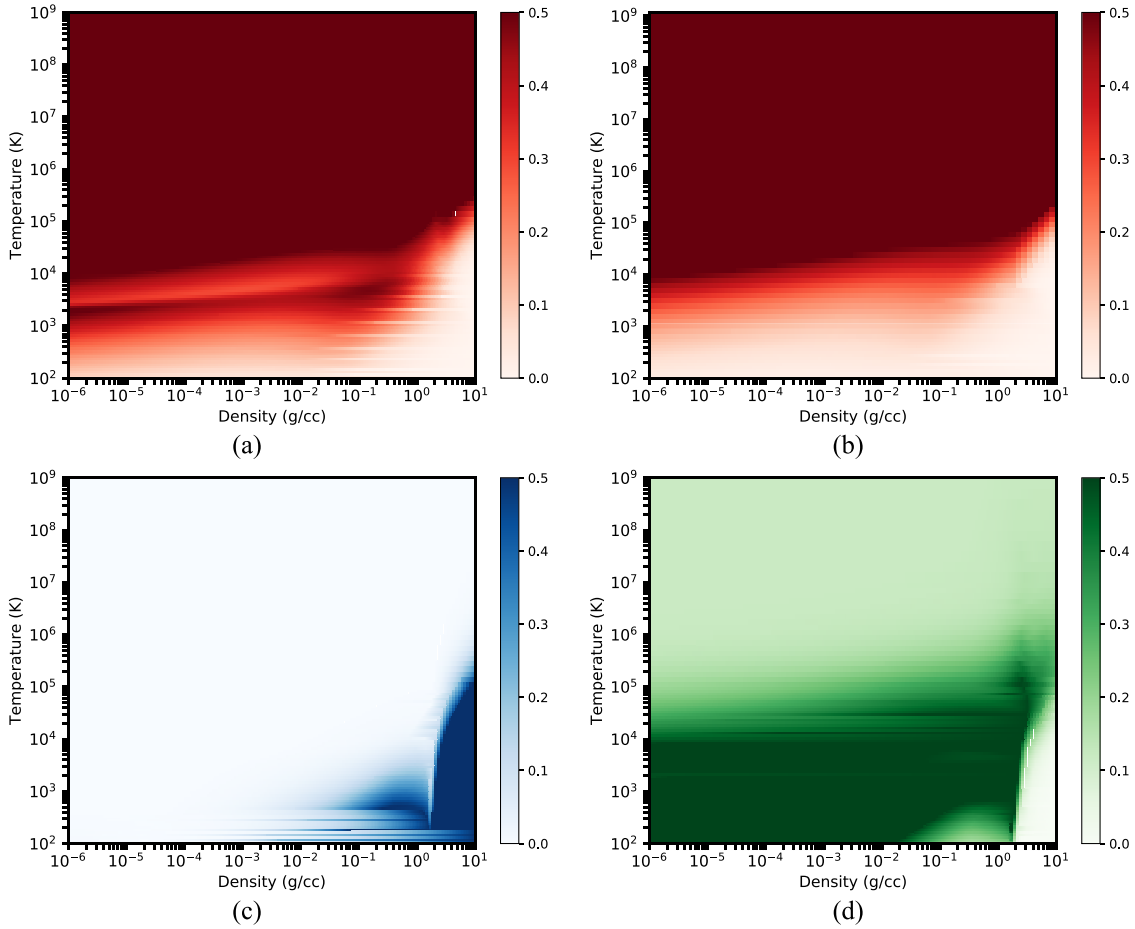

FIG. 2. Comparison of the three different contributions to the total pressure $P = -(\partial F/\partial V)_T = P_{\text{electron}} + P_{\text{cold}} + P_{\text{ion}}$: (a) the electron-thermal pressure $P_{\text{electron}} = -(\partial F_{\text{electron}}/\partial V)_T$ in our EOS; (b) the electron-thermal pressure from a different EOS (L2270) that we describe below which treats CO_2 as though it were composed of only the fictitious atomic species (C + 2O)/3 under all conditions (i.e., it neglects molecular CO_2 and the chemical transformation from the molecular, undissociated form to this atomic species); (c) the cold pressure $P_{\text{cold}} = -dF_{\text{cold}}/dV$ in our EOS; (d) the ion-thermal pressure $P_{\text{ion}} = -(\partial F_{\text{ion}}/\partial V)_T$ in our EOS. The pseudocolor depicts, for a given density and temperature, the fraction of the total pressure made by each contribution. The maximum pseudocolor scale is capped at 50% to accentuate the dominant regimes for each contribution.

of electronic excitations. In contrast, the cold curve [see Fig. 2(c)] is most important for low-to-moderate temperatures and compression regimes where bonding occurs more readily and electron degeneracy plays a big role. The ion-thermal contribution [Fig. 2(d)] matters most where motion of the nuclei is prominent, especially during dissociation, and in regions where F_{electron} and F_{cold} are small. Many of these regions correspond to low-density conditions where the system exists as a gas, although there are also condensed-phase conditions, particularly at higher temperatures, where the ion-thermal term makes a non-negligible contribution even when the electron-thermal term dominates.

At densities less than 1 g/cc, there is a dark band in Fig. 2(a) that appears at temperatures on the order of 10^3 K. The top of this band indicates temperatures where the onset of dissociation occurs (compare with Fig. 7), and the light-colored region immediately above this dark band indicates conditions where dissociation proceeds toward completion. The relative contribution made by the electron-thermal term is smaller in this light-colored region because the ion-thermal term makes a larger contribution than it otherwise would in the absence of dissociation. This can be seen by comparing Fig. 2(a) with Fig. 2(b); the light-colored region is absent in the latter figure because the L2270 EOS illustrated in it does not have a model that allows for transformation from molecular CO_2 to the dissociated atomic species.

The rest of this paper largely focuses on illustrating complications involved in the EOS-making procedure, discussing our resulting CO_2 EOS, and showing the impact of the dissociation model. Some experimental data are used to fit or constrain the EOS parameters, while others are used to validate our models. Here, we give

a brief overview of the types of data used to constrain the EOS. It should be understood first of all that the TF electron-thermal free energy contains no adjustable parameters, so only the cold and ion-thermal models provide some flexibility for fitting. The cold curve is heavily based upon experimental isotherms. The ion-thermal free energy includes both nondissociative and dissociative parts, which are coupled throughout the entire table range. Since experimental data for dissociation are severely lacking, we have fit our dissociation parameters to theoretical predictions. We have relied heavily on Cheetah[56–58] for the CO_2 fluid (liquid, vapor, and supercritical fluid) regimes depicted in Fig. 1 where bonding and electronic ionization are not significant. The nondissociative portion of the ion-thermal model was built iteratively together with the dissociation model to best reproduce data such as elevated-temperature isotherms, fluid-phase Hugoniot curves, and the solid–fluid phase boundary. While these different sets of data are used to constrain the parameters in the EOS, we reiterate the point that our aim is not necessarily to reproduce them perfectly but rather to provide an averaged representation as we will illustrate below. In fact, it is not possible to provide a close fit to all of the available data due to a number of reasons: (1) the model parameters available for fitting are far fewer in number than the available EOS constraints; (2) our models provide only an approximate, simplified description of reality; and (3) there might be some inconsistencies among the different sets of data. In Sec. III C, we demonstrate the impact of dissociation, focusing on quantities such as gas-phase Hugoniot curves that are heavily influenced by chemical reactions.

We have implemented the models described above into XEOS, which reads in the appropriate values of the parameters to generate a tabular version of our EOS. This tabular EOS is part of the Livermore Equation of State (LEOS) repository, and we refer to it in this paper as L2274. The table contains information about thermodynamic properties (e.g., total energies and pressures) at a series of discrete points in the density–temperature space in Fig. 1. In an effort to more clearly demonstrate the effect of chemical dissociation on the thermodynamic behavior, we compare results from L2274 to three existing CO_2 EOSs: L2270 and two SESAME tables, S5211 and S5212.[23,72]

The S5211 and L2270 tables are on opposite sides of the spectrum in terms of their dissociation behavior. S5211 neglects dissociation completely and is based on a description of CO_2 as a purely molecular system modeled by an effective exponential-six potential. As a result, it is intended only for relatively low pressures/densities and temperatures regions where dissociation or ionization are not significant. In contrast, L2270 is a global-range EOS that is based on the QEOS methodology typically used for metals. L2270 treats CO_2 as being fully dissociated over the entire (V, T) space, and it therefore underestimates the fluid and solid heat capacity. Other than the fact that the newer SESAME table, S5212, is based on the TF electron-thermal model, there is not much documentation on it, but the results in Sec. III C suggest that its dissociation behavior is similar to that of L2270. In some sense, none of these existing EOSs fully represent the behavior of a true dissociative CO_2 system. While there is still much room for improvement, our CO_2 L2274 EOS is able to capture the essence of the chemical transformation, which is the change in average molar mass $\bar{M}$. In Sec. III, we discuss and compare EOS behavior in several properties.

B. EOS constraints and comparisons

1. Isotherms

Figure 3 shows various room-temperature isotherms of the solid phases determined through experimental and theoretical methods. As we have explained above, these condensed-phase isotherms are largely determined by the cold curve in our EOS. The XEOS code used to generate our EOS allows for only one cold curve. It is clear from these figures that a single cold curve cannot provide a good representation of all the CO_2 solid phases over the entire density range shown in the figures. We cannot construct a curve that passes through both the molecular solids and the relatively low-pressure polymeric CO_2-V data reported by Yoo *et al.*[27] By applying a suitably chosen set of density breakpoints as described in Eq. (7), however, it is possible to fit a single cold curve to the molecular solids and to the higher-pressure CO_2-V data from Dzubiek *et al.*,[24] but we have chosen not to do that because the densities examined by Dzubiek *et al.* overlap with the densities spanned by a fluid-phase Hugoniot that we present later in this paper. The primary goal of our EOS is to provide a simplified, but still fairly illustrative representation of the complex dissociation behavior of CO_2 and the data to which we fit our dissociation models largely pertain to the supercritical-fluid phase, which has a density that more closely resembles those of the molecular solids than the polymeric solids. We would therefore not be able to obtain good agreement with the fluid-phase Hugoniot and calibrate our dissociation models if we chose to fit our EOS to the high-pressure Dzubiek *et al.* data on the polymeric solids.

Figure 4 shows the 2000 K fluid isotherm from Sterner and Pitzer,[73] which is the highest temperature that they examine with their EOS. Also illustrated in this figure is the same isotherm from Cheetah, which extends over a much wider range of conditions than that from Sterner and Pitzer. We have calibrated our EOS (the cold curve as well as the ion-thermal term) with both sets of data. Our cold curve is able to model both sets of fluid-phase results and provide an averaged representation of the molecular solids in Fig. 3 as well.

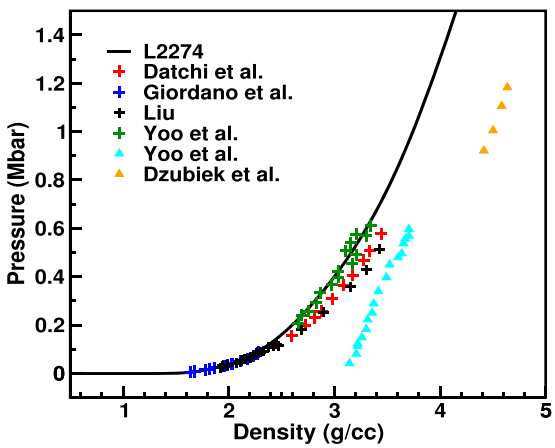

FIG. 3. Comparison of the 300 K isotherm of L2274 with representative experimental solid isotherms. Crosses and triangles represent measurements for molecular and polymeric solids, respectively.

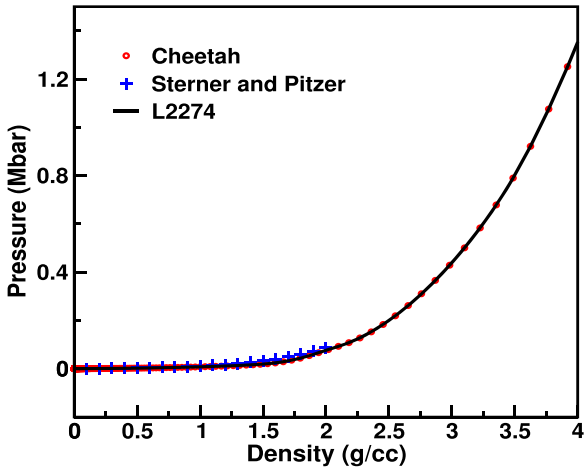

FIG. 4. Comparison of the 2000 K fluid-phase isotherm of L2274 with Cheetah and the CO_2 EOS of Sterner and Pitzer.[73]

For the CO_2 solids that are not part of our intended EOS constraints, L2274's performance depends on the particular solid phase. For instance, Fig. 5 shows about a 3% difference between the 726 K isotherm from L2274 and that reported by Giordano and Datchi,[47] who presented data for phases I, IV, and VII, all three of which are molecular solids. Thus, our EOS can reproduce the pressure–volume–temperature behavior of the molecular solids in an aggregate sense, but it is unable to account for the relatively small variations among the different phases that make up this category of solids. Note that L2270 which has the softest cold curve (has the lowest pressure for a given density), matches these data the best. However, the softer cold curve of L2270 also yields a fluid-phase Hugoniot that is too soft, as will be shown in Sec. III B 3). Overall, L2274 and S5211 perform reasonably well against the experimental data, while S5212 results in a considerably higher pressure than that observed experimentally.

Finally, for a much larger pressure range that encompasses the polymeric solids, we show a comparison between L2274, L2270, S5211 (limited to 4 Mbar), and S5212 with available isotherms in Fig. 6. The plot includes a few of the published isotherms for CO_2-V, as well as three other high-pressure polymeric solids observed by Lu *et al.*[74] in their DFT simulations: a tetrahedral phase with space group $P4_2/nmc$ that is predicted to be stable between 2.9 and 9.7 Mbar, a *Pbcn* sixfold-coordinated phase between 9.7 and 10.3 Mbar, and a $Pa\bar{3}$ sixfold-coordinated phase above 10.3 Mbar. The cold curve of S5212 is slightly stiffer (has a larger pressure for a given density) than that from L2274, while L2270 is significantly softer than L2274. The DFT cold curve was obtained a decade after the generation of L2270. It is clear from Fig. 6 that none of the EOSs have attempted to accurately model the polymeric solids. We discuss in the Conclusions how this issue may be addressed in the future by employing a multiphase EOS framework.

2. Chemical dissociation

This section illustrates in more detail the most distinctive feature of L2274, which is our dissociation model. The dissociation of CO_2 has been observed at pressures and temperatures above 0.40 Mbar and a few thousand kelvin, respectively, in the supercritical-fluid phase,[12,16,19,20,23] and at similar pressures but lower temperatures (roughly 1500–2500 K) in CO_2-V.[13–15,17,18] We do note, however, that some recent studies have questioned the notion that CO_2-V undergoes dissociation at conditions relevant to Earth's mantle. For instance, Dziubek *et al.* do not detect the presence of pure carbon (in the form of diamond) or oxygen from their X-ray diffraction and Raman analysis for pressures up to 0.85 Mbar and temperatures up to 2700 K. Since the polymeric solids are not specifically modeled *per se* in our EOS, we focus our attention on the chemistry of CO_2 fluid, which is less controversial.

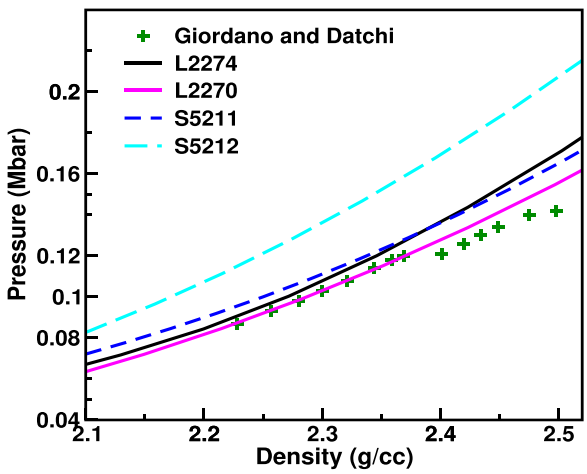

FIG. 5. Comparison of 726 K solid-phase isotherms produced from L2274, L2270, S5211, and S5212 with experimental data.[47]

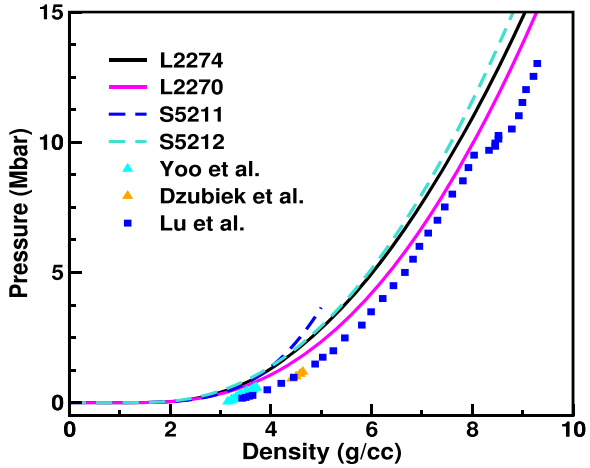

FIG. 6. Comparison of 300 K isotherms produced from L2274, L2270, S5211, and S5212 with solid isotherms from representative high-pressure experimental and theoretical studies.

Due to lack of experimental data to which we can calibrate our dissociation model, we rely largely on the predictions from Cheetah. This thermochemical code assumes that CO_2 dissociates into multiple chemical species: carbon monoxide (CO), atomic oxygen (O), molecular oxygen (O_2), ozone (O_3), and carbon (C) in the forms of the atomic, fluid, diamond, and graphite phases. Cheetah determines the equilibrium composition for a given pressure and temperature by minimizing the total Gibbs energy. It computes this free energy by modeling the interactions between the different species with dipolar exponential-six potentials.[75,76] Figures 7(a) and 7(b) display the relative concentrations of species predicted by Cheetah as a function of temperature along two distinct isochores (10^{-4} g/cc and 1 g/cc). Both densities are well within the applicability range of Cheetah. For higher densities (e.g., above 3 g/cc) where Cheetah is expected to become inaccurate, we rely on first-principles QMD simulations. However, we do not utilize QMD results of chemical-species analysis since defining molecular species in a condensed-matter environment is not a straightforward task. Instead, we constrain the EOS to QMD predictions of the total energies and pressures.

We have explained earlier that one of the most important effects of dissociation is to alter the average molar mass $\bar{M}$ defined in Eq. (25). It is clear that the simplified dissociation mechanism assumed by our EOS in (9) cannot reproduce the relative concentrations predicted by Cheetah's CO_2 dissociation mechanism involving multiple reactive species. Nonetheless, Figs. 7(c) and 7(d)

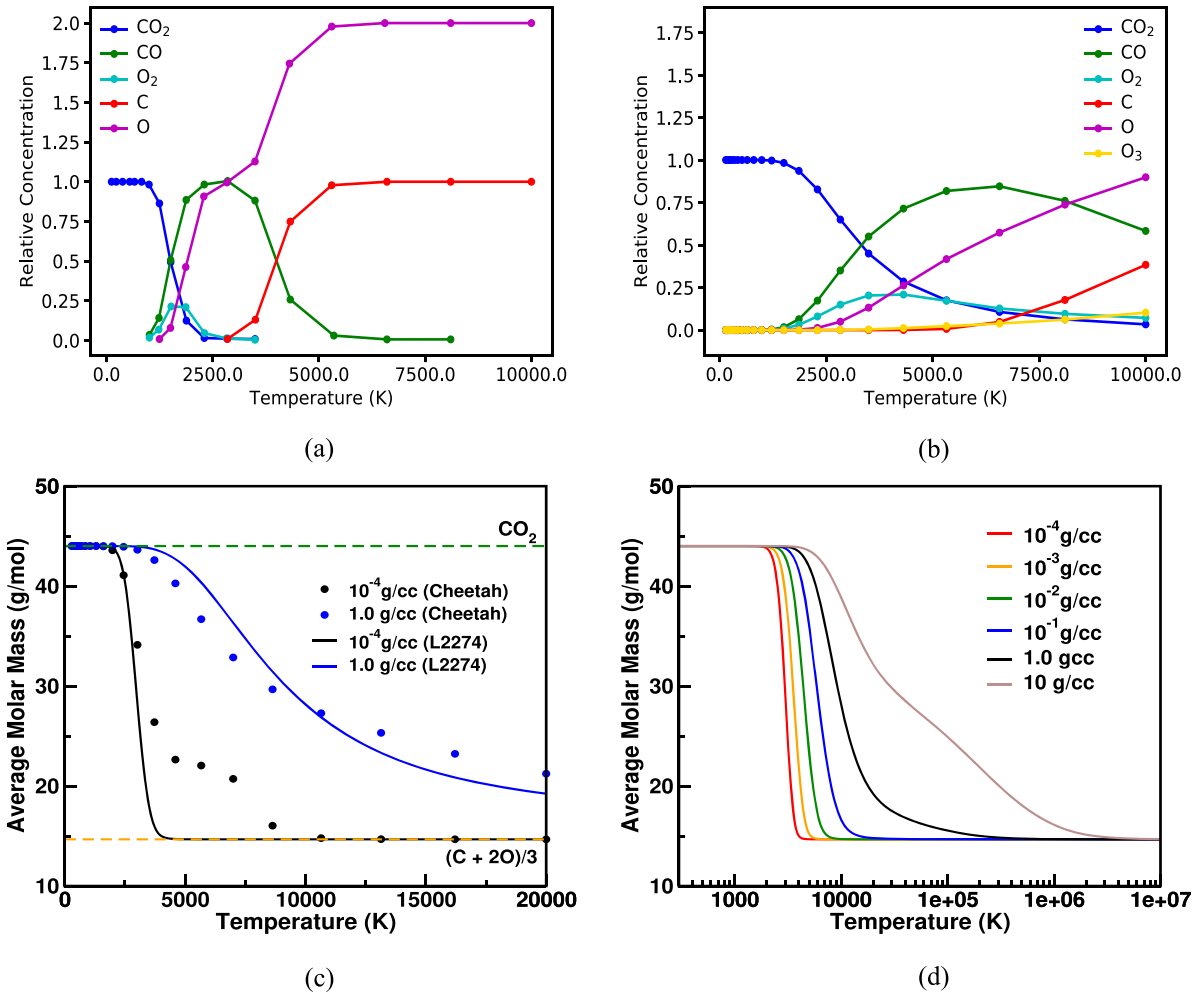

FIG. 7. Illustration of the effect of CO_2 dissociation: (a) Cheetah predictions for the change in the concentration of various species (relative to the concentration of CO_2 at 300 K) as a function of temperature along the 10^{-4} g/cc isochore in the gas phase; (b) similar to (a), except that this depicts the 1 g/cc isochore in the liquid/supercritical-fluid phases; (c) comparison between our EOS and Cheetah for the average molar mass $\bar{M}$ along the same two isochores in (a) and (b), where the green and orange dashed lines denote the upper (44 g/mol) and lower (44/3 = 14.7 g/mol) limits on $\bar{M}$, respectively; (d) our EOS predictions for $\bar{M}$ along several different isochores. We note that $\bar{M}$ in the dissociation-free S5211 table is always at the upper limit of 44 g/mol (CO_2), while $\bar{M}$ is always at the lower limit of 14.7 g/mol [(C + 2O)/3] in the full-dissociation-only L2270 table.

TABLE I. Parameters for the dissociative contribution $F_{ion,diss}(V, T)$ defined in (10) to the ion-thermal free energy $F_{ion}(V, T)$ in Eq. (8). The parameters include the rotational temperature Θ_{rot} that appears in the partition function $q_{rot,Y}$ in (18), frequencies of the four vibrational modes (two of which are degenerate) in the partition function $q_{vib,Y}$ in (22), and the dissociation energy ε_{diss} involved in the partition function $q_{diss,X}$ in (23).

Θ_{rot} (K)	Vibrational frequencies (cm^{-1})	ε_{diss} (eV)
0.561	954, 954, 1890, 3360	7.5

demonstrate that we can capture the essence of dissociation by tracking the change in $\bar{M}$. At low temperatures, CO_2 is completely undissociated so that $\bar{M}$ = 44 g/mol. The opposite extreme of complete dissociation is achieved at sufficiently high temperatures where only the atomic species (C + 2O)/3 is present and $\bar{M}$ = 44/3 = 14.7 g/mol. It is apparent that dissociation occurs more readily in dilute gases than in condensed phases. This is due to an entropic effect in which a higher volume favors formation of dissociated particles. Table I lists the values of the parameters in our dissociation model. We have set the rotational temperature Θ_{rot} to its gas-phase value and have also preserved the twofold degeneracy of one of the vibrational modes. In order to match Cheetah's predictions on the behavior of $\bar{M}$ in the liquid and supercritical fluid phases, we have found that it is necessary to modify the magnitude of the frequencies from those obtained by gas-phase spectroscopy.

3. Isobars, fluid-phase Hugoniot, and isochores

In addition to isotherms at elevated temperatures (e.g., Fig. 4), isobars and condensed-phase Hugoniot curves provide important sources of information to which we constrain our ion-thermal EOS model, especially the nondissociative part.

Figure 8 shows isobars from a fluid-phase EOS that Span and Wagner[55] have highly parameterized to a diverse variety of vapor, liquid, and supercritical data over pressures ranging from 0.5 to

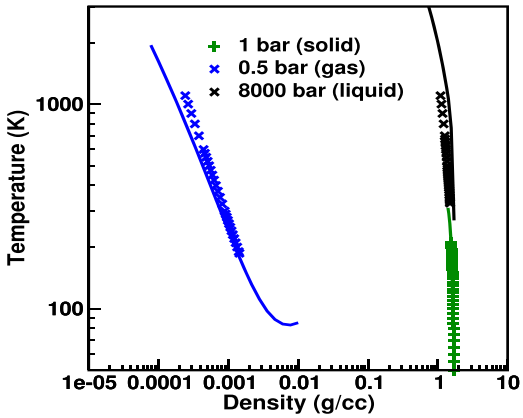

FIG. 8. Comparison of our EOS (solid curves) with experimental and theoretical results for different isobars: isobars from our EOS, vapor-phase (0.5 bar), and liquid/supercritical-fluid (8000 bar) isobars from the theoretical model of Span and Wagner,[55] and the ambient-pressure isobar for CO_2-I reported by Krupskii *et al.*[77] and Heit *et al.*[78]

8000 bar and temperatures up to 1100 K. The figure also includes results for the ambient-pressure isobar of CO_2-I. Overall, L2274 performs surprisingly well over this fairly wide range of pressures, given the simplicity of our model.

At higher pressures, CO_2 Hugoniot curves initiated from condensed-phase samples provide very useful constraints on the thermal models. Figure 9(a) depicts the Hugoniot pressure as a function of density obtained when CO_2 is cooled to a cryogenic liquid condition before being shocked to much higher densities and temperatures. Cryogenic CO_2 is optically transparent, but it becomes metallic under shock, making it possible for the optical measurements on the high-pressure, shocked state. At a pressure of about

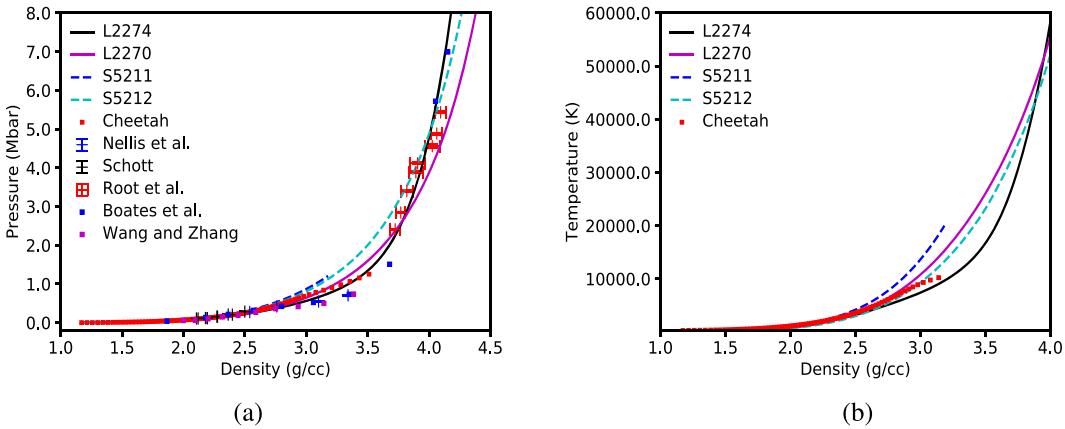

(a) (b)

FIG. 9. Results for a fluid-phase Hugoniot curve with an initial state of 1.17 g/cc and 218 K presented in terms of: (a) pressure as a function of density and (b) temperature vs density. The results illustrated here come from L2274, L2270, S5211, and S5212; three experimental studies;[16,12,23] two QMD studies;[19,20] and the Cheetah thermochemical code.[56–58]

0.4 Mbar, previous studies report a slope discontinuity in the Hugoniot (this discontinuity is difficult to see at the scale in the figures), which they attribute to the onset of dissociation. It is clear from Fig. 2 that the cold curve, in particular, makes a strong contribution to this fluid-phase Hugoniot in the regimes where the experimental data exist (i.e., densities and temperatures below 4 g/cc and 10^5 K, respectively.) As we have explained in Sec. III A, we employ an iterative procedure to optimize our cold curve together with the two parts of our ion-thermal model, the dissociative and nondissociative contributions [the latter is characterized by the Debye temperature $\Theta_D(V)$], to give an averaged representation of a diverse selection of data. The cold curve is largely constrained by the isotherms in Sec. III B 1, the dissociative contribution by Cheetah's predictions of chemical equilibria in Sec. III B 2, and the nondissociative contribution by the isobars, fluid-phase Hugoniot, and isochores in the present section.

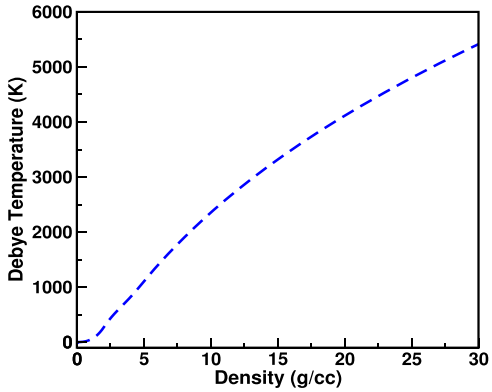

FIG. 10. The Debye temperature Θ_D in our EOS as a function of density.

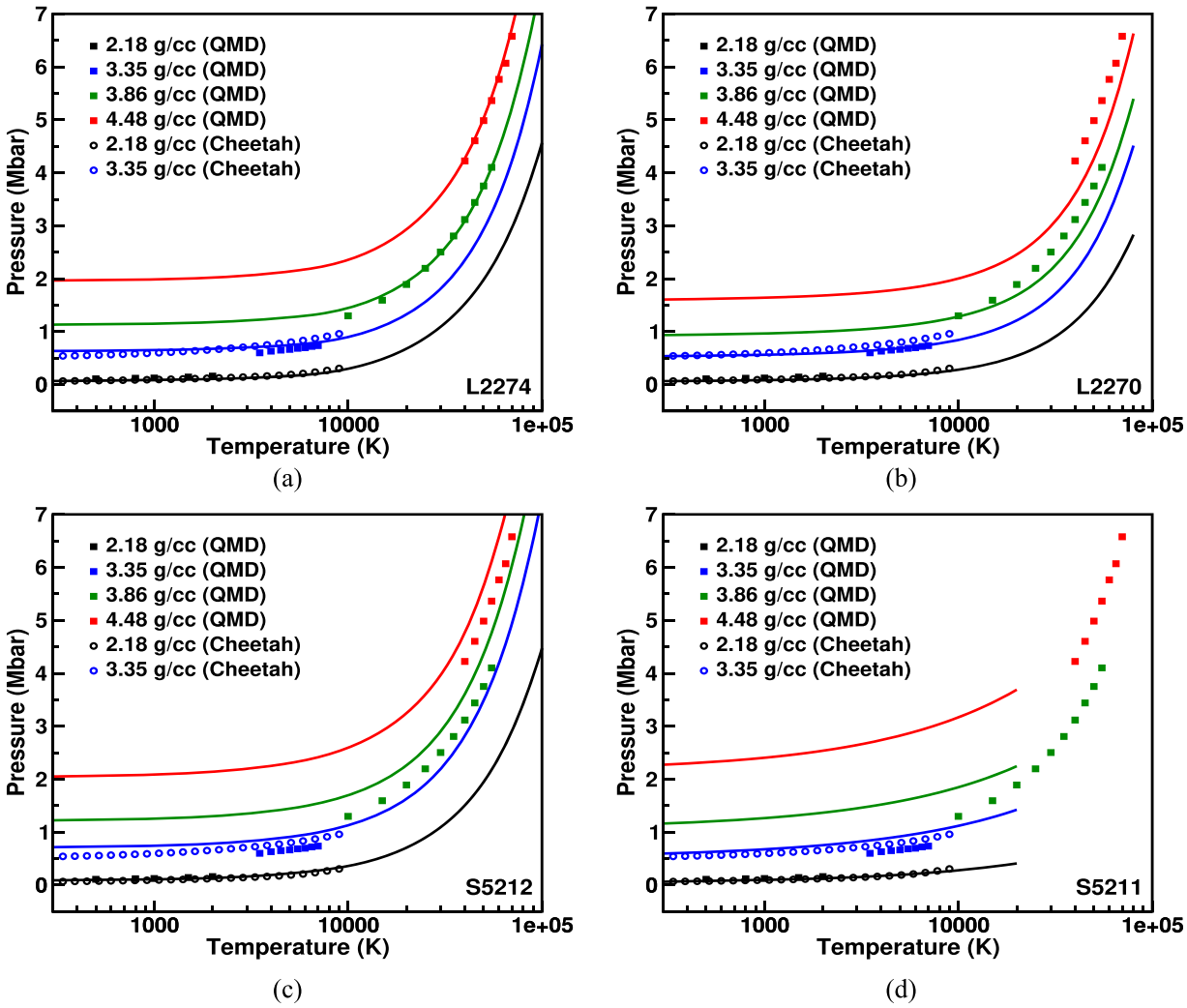

FIG. 11. Temperature vs pressure isochores for four EOSs: (a) L2274, (b) L2270, (c) S5212, and (d) S5211. Also included are QMD simulations from Boates *et al.*[20] and predictions from Cheetah[56–58] within its applicable density range.

Our EOS, L2274, generally agrees better with the data in Fig. 9(a) than do other EOSs. L2270 was developed over 20 years ago, before much of the fluid-phase Hugoniot data in Fig. 9 became available. Root *et al.*[23] have also compared predictions from L2274 and S5212 to their own shock-compression experiments and QMD simulations, and they have concluded that L2274 generally yields better agreement for the high-pressure results although they note that there are certain regions at lower pressure where S5212 seems to be more accurate. Comparing Fig. 9(b) with Fig. 9(a), we see that the differences between the EOSs are manifested much more profoundly in temperature–density space than in pressure–density space. Because it has a more realistic dissociation model, L2274 produces a Hugoniot that is substantially lower in temperature than the other three EOSs and is more consistent with the Cheetah predictions. For certain values of the density (e.g., at around 3.5 g/cc), the difference could be as large as 10^4 K. A more in-depth comparison of these EOSs to QMD predictions of Hugoniot temperatures will be provided in Sec. III C.

The nondissociative contribution to the ion-thermal free energy is iteratively optimized with the dissociation model constrained by the Cheetah results to reproduce the data mentioned above. The Debye and Cowan models, that characterize nondissociative contribution made by the solid and fluid phases, respectively, have one adjustable parameter: the Debye temperature Θ_D. We treat Θ_D as being independent of temperature, and Fig. 10 shows how it varies with density in our EOS. At the reference volume V_0 of 0.641 cc/g (corresponding to a reference density of 1.56 g/cc), Θ_D has a value of 139 K. The Grüneisen parameter Γ is related to Θ_D through the relation $\Gamma = -\mathrm{d}\ln\Theta_D/\mathrm{d}\ln V$, which leads to a value of $\Gamma = 2.616$ at $V = V_0$.

The isochores in Fig. 11 provide a set of data to validate our EOS because they were not used to fit the parameters. The figure compares isochores from the different EOSs with theoretical predictions from Cheetah and the QMD simulations by Boates *et al.*[20] The starting pressure at the lowest temperature (0 K) along each isochore is governed by the cold pressure. By definition, the volume is fixed along an isochore, and hence the cold energy is fixed along it as well. As a result, the isochore curvature $[(\partial P/\partial T)_V]$ is controlled by thermal contributions. It is important to note that we do not obtain perfect agreement with the Cheetah and QMD results because we have also fitted the ion-thermal free energy to other sources of data (such as the isobars and the Hugoniot curves presented above), and there are some inconsistencies among the different sets of data. Nevertheless, the overall agreement between L2274 and these theoretical predictions is excellent as shown in Fig. 11(a). L2274 agrees much better than the other three EOSs shown in Figs. 11(b)–11(d). Consistent with its isotherm behavior depicted in Fig. 5 and its Hugoniot behavior in Fig. 9, L2270 is accurate at low pressures but is too soft at higher pressures. Admittedly, L2270, S5211, and S5212 all predate and so could not benefit from the QMD results, which represent one of the few sets of data for the liquid and supercritical fluid at high temperatures and pressures where experimental data are virtually absent. Nevertheless, even if the QMD results were available at the

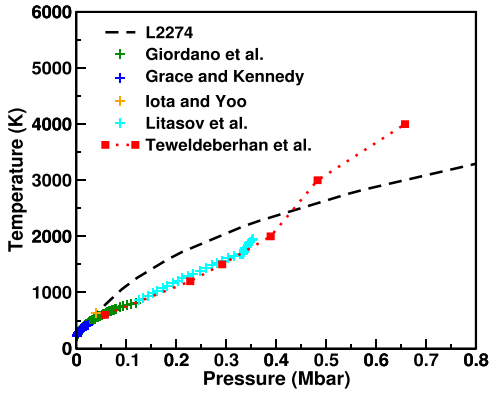

FIG. 12. The solid–fluid transition curve from our EOS (L2274) compared with experimental results from Grace and Kennedy,[79] Iota and Yoo,[40] Giordano *et al.*,[80] and Litasov *et al.*,[15] along with QMD predictions from Teweldeberhan *et al.*[22]

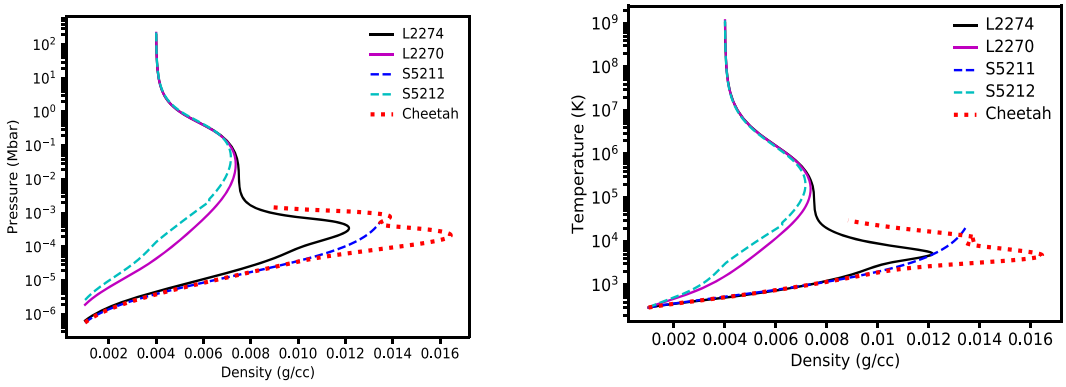

FIG. 13. Comparison of gas-phase Hugoniot curves shocked from an initial state of 0.001 g/cc and 300 K: (a) pressure vs density and (b) temperature vs density. The results illustrated here come from L2274, L2270, S5211, S5212, and Cheetah.[56–58]

time of development, we do not expect that the earlier EOSs would be able to reproduce them because of the limitations of their dissociation models (or the complete absence of such a model in the case of S5211).

4. Solid–fluid phase boundary

We have largely neglected liquid–vapor equilibria and related phenomena [the critical point and the liquid–vapor–solid (CO_2-I) triple point] in our study; although as explained in the Conclusions, this is an issue that we intend to address in the future. The only phase boundary we have examined in this work is the solid–fluid transition curve illustrated in Fig. 12. Depending on the pressure and temperature (e.g., CO_2 has an ambient-pressure sublimation temperature of 194.7 K and a critical point of 74 bar and 304.3 K), the fluid along that phase boundary could represent either vapor, liquid, or supercritical fluid. Out of all the studies cited in Fig. 12, the one that examines the lowest range of pressures is Grace and Kennedy,[79] who report results for pressures between 2 and 23 kbar, corresponding to temperatures between 216 and 420 K. Thus, nearly all of the data presented in Fig. 12 pertain to the supercritical fluid.

We model the solid–fluid transition curve with the Lindemann expression in Eq. (27). The Debye temperature $\Theta_D(V)$ that appears in this equation is already constrained (see Fig. 10) to the isotherm, isobar, and fluid-phase Hugoniot data described above. Thus, the only flexibility we have in adjusting the transition curve is to change the value of constant α in Eq. (27). We set α to agree with the melt temperature at the lowest pressure in the work of Grace and Kennedy (216 K). Although this phase boundary behaves reasonably in our EOS, a Lindemann expression is clearly not accurate for CO_2,

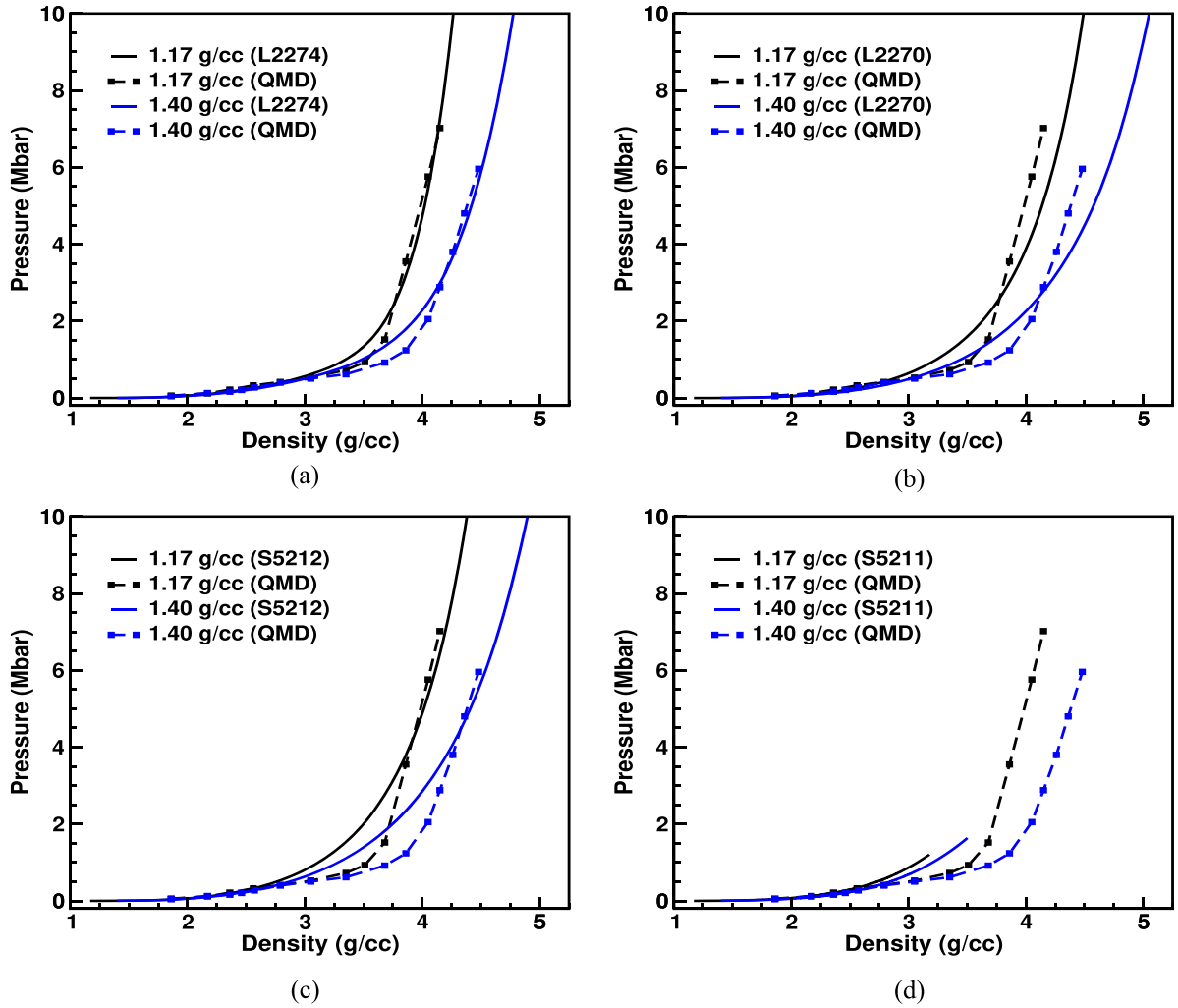

FIG. 14. Pressure vs density Hugoniot results for four EOSs: (a) L2274, (b) L2270, (c) S5212, and (d) S5211. Also included are QMD simulations from Boates *et al.*[20] Each figure shows results for two different Hugoniot curves initiated from a compressed liquid state that is at room temperature and at one of the two densities indicated by the labels.

and we explain in the Conclusions how we plan to rectify this issue in a future study.

C. Impact of chemical dissociation

The main distinguishing feature of our EOS lies in the dissociation model of the ion-thermal term. In this section, we discuss two types of thermodynamic data that are deemed to be sensitive to chemical reactions and are thus good choices for illustrating the impact of chemistry and for discriminating among the different EOSs: (1) gas-phase Hugoniot curves and (2) Hugoniot temperatures.

1. Gas-phase Hugoniot

Molecular compounds like CO_2 are known to exhibit significant dissociation under shock compression. The effect of dissociation is especially pronounced in Hugoniot curves initiated from gas samples, where the cold pressures for the low-density gas regime are small. Differences in the dissociation model among the EOSs will therefore be accentuated along these gas-phase curves. The Hugoniot generated from shocking a gas sample initially at 0.001 g/cc and 300 K is depicted in Fig. 13. The pseudocolor plots in Fig. 2 indicate that this gas-phase Hugoniot is, at least at temperatures below 10 000 K, controlled by the ion-thermal term and hence we expect dissociation to have a strong influence on the behavior at these temperatures.

From examining the average molar mass $\bar{M}$ along this Hugoniot in our EOS, we find that the onset of dissociation ($\bar{M}$ starts to deviate noticeably from 44 g/mol) at a density and temperature of about 0.009 g/cc and 2700 K, respectively. Below this temperature, CO_2 remains undissociated, and as a result, our EOS overlaps fairly well with S5211. This agreement at lower temperatures

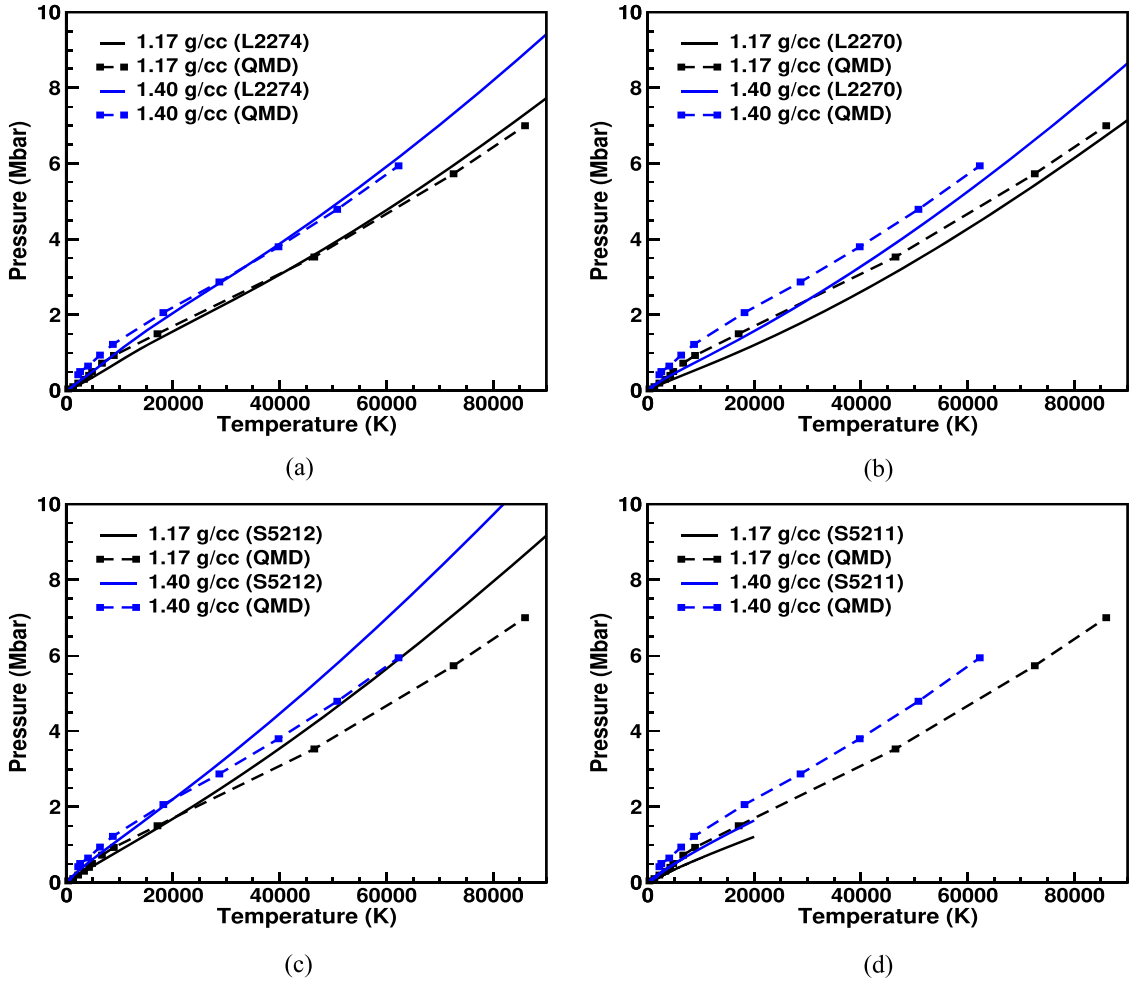

FIG. 15. Pressure vs temperature Hugoniot results for four EOSs: (a) L2274, (b) L2270, (c) S5212, and (d) S5211. Also included are QMD simulations from Boates *et al.*[20] Each figure shows results for two different Hugoniot curves initiated from a compressed liquid state that is at room temperature and at one of the two densities indicated by the labels.

is not surprising since S5211 treats CO_2 as a purely molecular (undissociated) system. Our EOS does not agree with L2270 or S5212 over these same conditions because, as we have explained in Sec. III A, L2270 and S5212 assume that CO_2 is completely dissociated at all conditions (including in the gas phase at ambient pressure), which consequently leads to an underestimation of the heat capacity and an overestimation of the temperature. All of this results in L2270 and S5212 underestimating the compressibility, meaning that they predict an overly low density or high specific volume.

At very high temperatures (e.g., above 10^7 K) where CO_2 is completely dissociated and the electron-thermal contribution dominates, the system becomes less compressible and the Hugoniot density moves back toward the ideal-gas limit of 4 times the density of the unshocked state (which is 0.004 g/cc in the case in Fig. 13). All of the EOSs agree well with each other in this electron-thermal-dominated regime, which is not surprising because they are all based on the Thomas–Fermi electron-thermal model described in Sec. II B. The behavior at both the low- and high-temperature limits is therefore expected based on our current models.

At intermediate temperatures (say, between 2700 and 7000 K), where CO_2 is neither fully dissociated nor undissociated, our EOS can represent, in a rough way, the rather complicated behavior that CO_2 may undergo. L2274 starts to deviate noticeably from S5211 at densities and temperatures above 0.009 g/cc and 2700 K due to the increasing prominence of dissociation. Furthermore, unlike L2270 or the two SESAME tables, our EOS exhibits a density maximum of 0.012 g/cc that occurs at a temperature of about 5000 K. The fact that L2274 exhibits a density maximum is due to dissociation. (It turns out that in our EOS, about half of the CO_2 molecules have dissociated at the density maximum.) When the dissociation is nearly complete, the gas, now largely monatomic, becomes less compressible and the Hugoniot density moves back toward the ideal-gas limit of 4 times the density of the unshocked state. The discrepancy between the L2274 and Cheetah shock-density maxima arises from differences in the dissociation behavior (Cheetah has a more complicated, multispecies reaction mechanism) and in the ionization behavior; the TF model in L2274 overestimates the extent of ionization, while Cheetah neglects ionization entirely.

We note that there is currently no experimental gas-phase Hugoniot data to validate the different EOSs. Perhaps a practical reason for this is because the low mechanical impedance of the gas (due to its low density) means that a very large energy input is required in order to shock it to high pressures; moreover, it is difficult to monitor the shock front of a dilute gas sample. The only data available come from Cheetah, which we have used to constrain our models. We encourage future experimental shock-compression studies on CO_2 in the gas phase to provide valuable data needed to constrain and validate the EOSs.

2. Hugoniot temperatures

As we have discussed in Sec. III B 3, the temperature along a Hugoniot curve is sensitive to the ion-thermal term of an EOS. Figures 14 and 15 illustrate results for two different Hugoniot curves in pressure–density and temperature–pressure space, respectively. Although not shown in the figures, the QMD results agree reasonably well with recent, soon-to-be-published data from Crandall *et al.*[81,82] The figures demonstrate that differences in the behavior of the various EOSs become amplified if one examines temperature instead of density. The temperatures from both S5212 and L2270 do not agree well with those from QMD. In contrast, L2274 is able to match the QMD results in terms of both density and temperature, despite the fact that we have not fit our parameters to these results. This good agreement is largely due to the inclusion of a more accurate chemical-dissociation model in our EOS.

IV. CONCLUSIONS

We have developed the first global CO_2 EOS that allows for the establishment of chemical equilibrium between the undissociated and dissociated forms. The inclusion of chemical equilibria is a largely unexplored topic in the development of EOSs for condensed-matter science. Our dissociation model contributes to the ion-thermal free energy, and it involves the rather simple reaction in (9), where CO_2 dissociates as though it were an ideal gas into the fictitious atomic species (C + 2O)/3. Despite this great simplification, our EOS is able to largely capture the trend predicted by the specialized thermochemical code Cheetah regarding the change in the average molar mass $\bar{M}$ as a function of density and temperature. Allowing $\bar{M}$ to vary in a nontrivial manner reflects the extent of the dissociation and is the most significant feature of the EOS. The differences between the EOSs are especially pronounced along gas-phase Hugoniot curves. In addition to shock Hugoniots, we have examined a diverse selection of data, including isotherms, isochores, isobars, and phase transitions from solid to fluid. The data to which we have fit our EOS cover a wide range of conditions spanning from dilute gases at ambient conditions (or at even lower pressures and temperatures) to condensed phases at hot, pressurized states that approach roughly 10^5 K and several megabars, making this EOS suitable for a number of different applications.

Despite the successes of our EOS, there is still much room for further improvement. The EOS involves a single cold (energy) curve. This is problematic for CO_2 because it means that we cannot accurately model both the polymeric solids (e.g., phases V and VI) and the molecular solids (phases I–IV and VII) over all of the density conditions shown in Figs. 3 and 6. For reasons explained in the main text, we have chosen to favor the molecular solids. We will address this issue in a future study by adopting a true multiphase framework where each phase is described by a separate cold energy and ion-thermal free energy. This would enable us to model both classes of solids and reproduce, in an aggregate sense, the isotherms in Figs. 3 and 6. The multiphase framework will also allow us to go beyond a Lindemann prescription of melting and improve the fidelity in certain regions (e.g., liquid–vapor equilibria) of the CO_2 phase diagram. In addition, the description of the electron-thermal free energy could be improved by switching from Thomas–Fermi to Purgatorio,[83,84] the latter of which provides an explicit treatment of the electronic shell structure through an average-atom-in-jellium approach. An even more accurate alternative to these electronic-structure methods would be to employ recent first-principles approaches[85] that have shown great promise for simulating extreme conditions that are inaccessible to traditional, orbital-based DFT methods. Finally,

one could further improve the dissociation model itself, with one possibility being to embed a thermochemical code like Cheetah into the EOS directly.

ACKNOWLEDGMENTS

This work was performed under the auspices of the U.S. Department of Energy by Lawrence Livermore National Laboratory under Contract No. DE-AC52-07NA27344. The authors thank L. E. Fried and S. Bastea for sharing their expertise on Cheetah; L. Crandall, J. R. Rygg, G. W. Collins, T. R. Boehly, A. Jenei, D. E. Fratanduono, M. C. Gregor, J. H. Eggert, M. Millot, and D. Spaulding for sending their unpublished shock-compression data on precompressed CO_2; S. Root for helpful discussions on shock Hugoniot curves of CO_2; and C. J. Prisbrey for her timely assistance in manuscript preparation.

REFERENCES

[1] W. J. Carter and S. P. Marsh, "Hugoniot equation of state of polymers," Technical Report LA-13006-MS, Los Alamos National Laboratory, 1995.
[2] J. L. Jordan, D. M. Dattelbaum, G. Sutherland, D. W. Richards, S. A. Sheffield, and R. D. Dick, "Shock equation of state of a multi-phase epoxy-based composite (Al–MnO_2-epoxy)," J. Appl. Phys. **107**, 103528 (2010).
[3] K. A. Maerzke, J. D. Coe, D. A. Fredenburg, J. M. Lang, and D. M. Dattelbaum, "Equations of state and shock-driven chemistry in poly(dimethylsiloxane)-based foams," AIP Conf. Proc. **1979**, 090009 (2018).
[4] K. A. Maerzke, J. D. Coe, C. Ticknor, J. A. Leiding, J. T. Gammel, and C. F. Welch, "Equations of state for polyethylene and its shock-driven decomposition products," J. Appl. Phys. **126**, 045902 (2019).
[5] D. A. Young and E. M. Corey, "A new global equation of state model for hot, dense matter," J. Appl. Phys. **78**, 3748–3755 (1995).
[6] K. Caldeira and M. R. Rampino, "Carbon dioxide emissions from Deccan volcanism and a K/T boundary greenhouse effect," Geophys. Res. Lett. **17**, 1299–1302, https://doi.org/10.1029/gl017i009p01299 (1990).
[7] J. D. Figueroa, T. Fout, S. Plasynski, H. McIlvried, and R. D. Srivastava, "Advances in CO_2 capture technology—The U.S. Department of Energy's carbon sequestration program," Int. J. Greenhouse Gas Control **2**, 9–20 (2008).
[8] Core Writing Team, R. K. Pachauri, and L. A. Meyer, "Climate change 2014: Synthesis report. Contribution of working groups I, II and III to the fifth assessment report of the intergovernmental panel on climate change," Technical Report, IPCC, Geneva, Switzerland, 2014, p. 151. See https://www.ipcc.ch/report/ar5/syr/.
[9] P. C. Myint and A. Firoozabadi, "Onset of convection with fluid compressibility and interface movement," Phys. Fluids **25**, 094105 (2013).
[10] A. Firoozabadi and P. C. Myint, "Prospects for subsurface CO_2 sequestration," AIChE J. **56**, 1398–1405 (2010).
[11] M. van Thiel and F. H. Ree, "Properties of carbon clusters in TNT detonation products: Graphite–diamond transition," J. Appl. Phys. **62**, 1761–1767 (1987).
[12] W. J. Nellis, A. C. Mitchell, F. H. Ree, M. Ross, N. C. Holmes, R. J. Trainor, and D. J. Erskine, "Equation of state of shock-compressed liquids: Carbon dioxide and air," J. Chem. Phys. **95**, 5268–5272 (1991).
[13] Y. Seto, D. Hamane, T. Nagai, and K. Fujino, "Fate of carbonates within oceanic plates subducted to the lower mantle, and a possible mechanism of diamond formation," Phys. Chem. Miner. **35**, 223–229 (2008).
[14] Y. Seto, D. Nishio-Hamane, T. Nagai, N. Sata, and K. Fujino, "Synchrotron X-ray diffraction study for crystal structure of solid carbon dioxide CO_2-V," J. Phys.: Conf. Ser. **215**, 012015 (2010).
[15] K. D. Litasov, A. F. Goncharov, and R. J. Hemley, "Crossover from melting to dissociation of CO_2 under pressure: Implications for the lower mantle," Earth Planet. Sci. Lett. **309**, 318–323 (2011).
[16] G. L. Schott, "Shock-compressed carbon dioxide: Liquid measurements and comparisons with selected models," High Pressure Res. **6**, 187–200 (1991).
[17] O. Tschauner, H.-K. Mao, and R. J. Hemley, "New transformations of CO_2 at high pressures and temperatures," Phys. Rev. Lett. **87**, 075701 (2001).
[18] A. R. Oganov, S. Ono, Y. Ma, C. W. Glass, and A. Garcia, "Novel high-pressure structures of $MgCO_3$, $CaCO_3$ and CO_2 and their role in Earth's lower mantle," Earth Planet. Sci. Lett. **273**, 38–47 (2008).
[19] C. Wang and P. Zhang, "Thermophysical properties of liquid carbon dioxide under shock compressions: Quantum molecular dynamic simulations," J. Chem. Phys. **133**, 134503 (2010).
[20] B. Boates, S. Hamel, E. Schwegler, and S. A. Bonev, "Structural and optical properties of liquid CO_2 for pressures up to 1 TPa," J. Chem. Phys. **134**, 064504 (2011).
[21] B. Boates, A. M. Teweldeberhan, and S. A. Bonev, "Stability of dense liquid carbon dioxide," Proc. Natl. Acad. Sci. U. S. A. **109**, 14808–14812 (2012).
[22] A. M. Teweldeberhan, B. Boates, and S. A. Bonev, "CO_2 in the mantle: Melting and solid–solid phase boundaries," Earth Planet. Sci. Lett. **373**, 228–232 (2013).
[23] S. Root, K. R. Cochrane, J. H. Carpenter, and T. R. Mattsson, "Carbon dioxide shock and reshock equation of state data to 8 Mbar: Experiments and simulations," Phys. Rev. B **87**, 224102 (2013).
[24] K. F. Dzubiek, M. Ende, D. Scelta, R. Bini, M. Mezouar, G. Garbarino, and R. Miletich, "Crystalline polymeric carbon dioxide stable at megabar pressures," Nat. Commun. **9**, 3148 (2018).
[25] V. Iota, C. S. Yoo, and H. Cynn, "Quartzlike carbon dioxide: An optically nonlinear extended solid at high pressures and temperatures," Science **283**, 1510–1513 (1999).
[26] S. Serra, C. Cavazzoni, G. L. Chiarotti, S. Scandolo, and E. Tosatti, "Pressure-induced solid carbonates from molecular CO_2 by computer simulation," Science **284**, 788–790 (1999).
[27] C. S. Yoo, H. Cynn, F. Gygi, G. Galli, V. Iota, M. Nicol, S. Carlson, D. Häusermann, and C. Mailhiot, "Crystal structure of carbon dioxide at high pressure: "Superhard" polymeric carbon dioxide," Phys. Rev. Lett. **83**, 5527–5530 (1999).
[28] J. Dong, J. K. Tomfohr, and O. F. Sankey, "Non-molecular carbon dioxide (CO_2) solids," Science **287**, 11 (2000).
[29] J. Dong, J. K. Tomfohr, O. F. Sankey, K. Leinenweber, M. Somayazulu, and P. F. McMillan, "Investigation of hardness in tetrahedrally bonded nonmolecular CO_2 solids by density-functional theory," Phys. Rev. B **62**, 14685 (2000).
[30] B. Holm, R. Ahuja, A. Belonoshko, and B. Johansson, "Theoretical investigation of high pressure phases of carbon dioxide," Phys. Rev. Lett. **85**, 1258–1261 (2000).
[31] J. Sun, D. D. Klug, R. Martoňák, J. Antonio Montoya, M.-S. Lee, S. Scandolo, and E. Tosatti, "High-pressure polymeric phases of carbon dioxide," Proc. Natl. Acad. Sci. U. S. A. **106**, 6077–6081 (2009).
[32] F. Datchi, B. Mallick, A. Salamat, and S. Ninet, "Structure of polymeric carbon dioxide CO_2-V," Phys. Rev. Lett. **108**, 125701 (2012).
[33] M. Santoro, F. A. Gorelli, R. Bini, J. Haines, O. Cambon, C. Levelut, J. A. Montoya, and S. Scandolo, "Partially collapsed cristobalite structure in the non molecular phase V in CO_2," Proc. Natl. Acad. Sci. U. S. A. **109**, 5176–5179 (2012).
[34] B. Olinger, "The compression of solid CO_2 at 296 K to 10 GPa," J. Chem. Phys. **77**, 6255–6258 (1982).
[35] L.-G. Liu, "Dry ice II, a new polymorph of CO_2," Nature **303**, 508–509 (1983).
[36] L.-G. Liu, "Compression and phase behavior of solid CO_2 to half a megabar," Earth Planet. Sci. Lett. **71**, 104–110 (1984).
[37] B. Kuchta and R. D. Etters, "Prediction of a high-pressure phase transition and other properties of solid CO_2 at low temperatures," Phys. Rev. B **38**, 6265–6269 (1988).
[38] K. Aoki, H. Yamawaki, M. Sakashita, Y. Gotoh, and K. Takemura, "Crystal structure of the high-pressure phase of solid CO_2," Science **263**, 356–358 (1994).
[39] H. Olijnyk and A. P. Jephcoat, "Vibrational studies on CO_2 up to 40 GPa by Raman spectroscopy at room temperature," Phys. Rev. B **57**, 879–888 (1998).
[40] V. Iota and C.-S. Yoo, "Phase diagram of carbon dioxide: Evidence for a new associated phase," Phys. Rev. Lett. **86**, 5922–5925 (2001).
[41] C.-S. Yoo, V. Iota, and H. Cynn, "Nonlinear carbon dioxide at high pressures and temperatures," Phys. Rev. Lett. **86**, 444–447 (2001).
[42] C. S. Yoo, H. Kohlmann, H. Cynn, M. F. Nicol, V. Iota, and T. LeBihan, "Crystal structure of pseudo-six-fold carbon dioxide phase II at high pressures and temperatures," Phys. Rev. B **65**, 104103 (2002).

[43]S. A. Bonev, F. Gygi, T. Ogitsu, and G. Galli, "High-pressure molecular phases of solid carbon dioxide," Phys. Rev. Lett. **91**, 065501 (2003).
[44]J.-H. Park, C. S. Yoo, V. Iota, H. Cynn, M. F. Nicol, and T. Le Bihan, "Crystal structure of bent carbon dioxide phase IV," Phys. Rev. B **68**, 014107 (2003).
[45]M. Santoro, J.-F. Lin, H.-K. Mao, and R. J. Hemley, "*In situ* high *P–T* Raman spectroscopy and laser heating of carbon dioxide," J. Chem. Phys. **121**, 2780–2787 (2004).
[46]M. Santoro and F. A. Gorelli, "High pressure solid state chemistry of carbon dioxide," Chem. Soc. Rev. **35**, 918–931 (2006).
[47]V. M. Giordano and F. Datchi, "Molecular carbon dioxide at high pressure and high temperature," Europhys. Lett. **77**, 46002 (2007).
[48]V. M. Giordano, F. Datchi, F. A. Gorelli, and R. Bini, "Equation of state and anharmonicity of carbon dioxide phase I up to 12 GPa and 800 K," J. Chem. Phys. **133**, 144501 (2010).
[49]J. P. M. Trusler, "Equation of state for solid phase I of carbon dioxide valid for temperatures up to 800 K and pressures up to 12 GPa," J. Phys. Chem. Ref. Data **40**, 043105 (2011).
[50]A. Sengupta, M. Kim, C.-S. Yoo, and J. S. Tse, "Polymerization of carbon dioxide: A chemistry view of molecular-to-nonmolecular phase transitions," J. Phys. Chem. C **116**, 2061–2067 (2012).
[51]S. Gohr, S. Grimme, T. Söhnel, B. Paulus, and P. Schwerdtfeger, "Pressure dependent stability and structure of carbon dioxide—A density functional study including long-range corrections," J. Chem. Phys. **139**, 174501 (2013).
[52]F. Datchi, B. Mallick, A. Salamat, G. Rousse, S. Ninet, G. Garbarino, P. Bouvier, and M. Mezouar, "Structure and compressibility of the high-pressure molecular phase II of carbon dioxide," Phys. Rev. B **89**, 144101 (2014).
[53]W. Sontising, Y. N. Heit, J. L. McKinley, and G. J. O. Beran, "Theoretical predictions suggest carbon dioxide phases III and VII are identical," Chem. Sci. **8**, 7374–7382 (2017).
[54]Y. Han, J. Liu, L. Huang, X. He, and J. Li, "Predicting the phase diagram of solid carbon dioxide at high pressure from first principles," npj Quantum Mater. **4**, 10 (2019).
[55]R. Span and W. Wagner, "A new equation of state for carbon dioxide covering the fluid region from the triple-point temperature to 1100 K at pressures up to 800 MPa," J. Phys. Chem. Ref. Data **25**, 1509–1596 (1996).
[56]L. E. Fried and P. C. Souers, "CHEETAH: A next generation thermochemical code," Technical Report UCRL-ID-117240, Lawrence Livermore National Laboratory, 1994.
[57]Cheetah thermochemical code, Lawrence Livermore National Laboratory, 2019.
[58]L. E. Fried and W. M. Howard, "An accurate equation of state for the exponential-6 fluid applied to dense supercritical nitrogen," J. Chem. Phys. **109**, 7338–7348 (1998).
[59]R. M. More, K. H. Warren, D. A. Young, and G. B. Zimmerman, "A new quotidian equation of state (QEOS) for hot dense matter," Phys. Fluids **31**, 3059–3078 (1988).
[60]D. A. Young, *Phase Diagrams of the Elements* (University of California Press, Berkeley, Los Angeles, 1991).
[61]V. N. Zubarev and G. S. Telegin, "Impact compressibility of liquid nitrogen and solid carbon dioxide," Dokl. Akad. Nauk SSSR **142**, 309–312 (1962) (in Russian).
[62]J.-P. Poirier, *Introduction to the Physics of the Earth's Interior*, 2nd ed. (Cambridge University Press, Cambridge, 2000).
[63]S. I. Sandler, *An Introduction to Applied Statistical Thermodynamics* (John Wiley & Sons, Hoboken, 2011).
[64]F. A. Gorelli, V. M. Giordano, P. R. Salvi, and R. Bini, "Linear carbon dioxide in the high-pressure high-temperature crystalline phase IV," Phys. Rev. Lett. **93**, 205503 (2004).
[65]F. Datchi, V. M. Giordano, P. Munsch, and A. M. Saitta, "Structure of carbon dioxide phase IV: Breakdown of the intermediate bonding state scenario," Phys. Rev. Lett. **103**, 185701 (2009).
[66]C.-S. Yoo, A. Sengupta, and M. Kim, "Phase diagram of carbon dioxide: Update and challenges," High Pressure Res. **31**, 68–74 (2011).
[67]F. Datchi and G. Weck, "X-ray crystallography of simple molecular solids up to megabar pressures: Application to solid oxygen and carbon dioxide," Z. Kristallogr. **229**, 135–157 (2014).
[68]R. Menikoff, "Empirical equations of state for solids," in *Shock Wave Science and Technology Reference Library* (Springer-Verlag, Berlin, Heidelberg, 2007), Chap. 4, pp. 143–188.
[69]S. H. Simon, *The Oxford Solid State Basics* (Oxford University Press, Oxford, 2013).
[70]C. W. Cranfill and R. M. More, "IONEOS: A fast, analytic, ion equation-of-state routine," Technical Report LA-7313-MS, Los Alamos Scientific Laboratory, 1978.
[71]F. A. Lindemann, "The calculation of molecular vibration frequencies," Phys. Z. **11**, 609–612 (1910) (in German).
[72]S. Root, J. H. Carpenter, K. R. Cochrane, and T. R. Mattsson, "Equation of state of CO_2: Experiments on Z, density functional theory (DFT) simulations, and tabular models," Technical Report SAND2012-8468, Sandia National Laboratories, 2012.
[73]S. M. Sterner and K. S. Pitzer, "An equation of state for carbon dioxide valid from zero to extreme pressures," Contrib. Mineral. Petrol. **117**, 362–374 (1994).
[74]C. Lu, M. Miao, and Y. Ma, "Structural evolution of carbon dioxide under high pressure," J. Am. Chem. Soc. **135**, 14167–14171 (2013).
[75]S. Bastea and L. E. Fried, "Exp6-polar thermodynamics of dense supercritical water," J. Chem. Phys. **128**, 174502 (2008).
[76]S. Bastea and L. E. Fried, "Chemical equilibrium detonation," in *Shock Waves Science and Technology Library*, Detonation Dynamics Vol. 6 (Springer, Berlin, 2012), Chap. 1, pp. 1–32.
[77]I. N. Krupskii, A. I. Prokhvatilov, A. I. Erenburg, and A. S. Barylnik, "Thermal expansion X-ray studies of solid CO_2," Fiz. Nizk. Temp. **8**, 533–541 (1982) (in Russian).
[78]Y. N. Heit, K. D. Nanda, and G. J. O. Beran, "Predicting finite-temperature properties of crystalline carbon dioxide from first principles with quantitative accuracy," Chem. Sci. **7**, 246–255 (2016).
[79]J. D. Grace and G. C. Kennedy, "The melting curve of five gases to 30 kb," J. Phys. Chem. Solids **28**, 977–982 (1967).
[80]V. M. Giordano, F. Datchi, and A. Dewaele, "Melting curve and fluid equation of state of carbon dioxide at high pressure and high temperature," J. Chem. Phys. **125**, 054504 (2006).
[81]L. Crandall, J. R. Rygg, G. W. Collins, T. R. Boehly, A. Jenei, D. E. Fratanduono, M. C. Gregor, J. H. Eggert, M. Millot, and D. Spaulding, "Equation-of-state measurements of precompressed CO_2 shocked to 10 Mbar," in Annual Meeting of the APS Division of Plasma Physics, Milwaukee, WI, USA, 2017.
[82]G. W. Collins, L. Crandall, J. R. Rygg, and D. E. Fratanduono, private communication, email correspondence regarding unpublished CO_2 shock-compression results (2019).
[83]B. Wilson, V. Sonnad, P. Sterne, and W. Isaacs, "Purgatorio—A new implementation of the Inferno algorithm," J. Quant. Spectrosc. Radiat. Transfer **99**, 658–679 (2006).
[84]P. A. Sterne, S. B. Hansen, B. G. Wilson, and W. A. Isaacs, "Equation of state, occupation probabilities and conductivities in the average atom Purgatorio code," High Energy Density Phys. **3**, 278–282 (2007).
[85]P. Suryanarayana, P. P. Pratapa, A. Sharma, and J. E. Pask, "SQDFT: Spectral Quadrature method for large-scale parallel $\mathcal{O}(n)$ Kohn–Sham calculations at high temperature," Comput. Phys. Commun. **224**, 288–298 (2018).